International Journal of Impact Engineering 144 (2020) 103586

Contents lists available at ScienceDirect

International Journal of Impact Engineering

journal homepage: www.elsevier.com/locate/ijimpeng

# Modelling and Analyses of Fiber Fabric and Fabric-Reinforced Polymers under Hypervelocity Impact Using Smooth Particle Hydrodynamics

Shicao Zhao (Numerical simulations)[a], Zhenfei Song (Data analyses and writing the paper)[b,c,*], Horacio D. Espinosa (Data Analyses)[c]

[a] Institute of Applied Computer, China Academy of Engineering Physics, Mianyang, 621900, P.R. China
[b] Institute of Fluid Physics, China Academy of Engineering Physics, Mianyang, 621900, P.R. China
[c] Mechanical Engineering Department, Northwestern University, Evanston, IL, 60201, USA

ARTICLE INFO

*Keywords:*
Smooth particle hydrodynamics
hypervelocity impact
fiber composite
fabric reinforced polymer
shielding performance

ABSTRACT

In a hypervelocity impact (HVI) event, fiber fabrics and the fabric-reinforced polymers (FRP) would undergo shock compression, large deformation and fragmentation. The smooth particle hydrodynamics (SPH) approach was applied to assess the shielding performance of the fabric and its composite structure in a Whipple shield. In the fabric model, a fiber is built by SPH particles to properly reproduce the spreading feature of fragmented fabric under HVI. The simulations display that an aluminum panel, serving as the bumper of a Whipple, has the better performance in debris spreading than fabric layers. In the stuffed layer of a Whipple, the widely used plain weave fabric has the similar performance as the 3D weave both in debris spreading and speed retarding. The fabric model is further developed and extended to FRP by building fiber and polymer materials separately based on specific geometries. The computations illustrate that the FRP/Aluminum hybrid laminate can efficiently reduce the shock peak under HVI and meanwhile produce large deformation for kinetic energy absorption, in good agreement with experimental measurements. It applies to the rear wall of a Whipple which should resist the HVI of a debris cloud, forming a high but short shock pulse. The further optimization of the hybrid laminate was made by using a corrugated aluminum plate, a gap and a Kevlar fabric layer, leading to the considerable reduction of the laminate areal mass in a prescribed thickness.

## 1. Introduction

Advanced fibers employed in woven fabrics, such as ceramic fibers, Kevlar, and Vectran [1–3], have been widely applied as reinforcing materials in spacecraft shields resisting HVI of space debris. In an enhanced Whipple shield [4,5], the Nextel and Kevlar fabrics were adopted instead of light-weight aluminum alloys. The characterization of the dynamic behaviors of such fabrics is done by planar impact testing to obtain its high-pressure equation of state [6], and by ballistic testing to validate damage models. The quantitative description of their damage behaviors including fracture and fragmentation in a HVI event, however, is still difficulty both in experimental diagnostic and data analyses. Numerical simulations, based on calibrated models, offer an efficient and direct way for selection of fibers and woven pattern, and for preliminary evaluation of the performance of specific fabrics.

In a fabric layer like the Nextel, a woven yarn is a collection of a bundle of fibers that have the diameter of only several micrometers. It poses a challenge to model the complex structure at a full scale. The yarn was simply treated as spring-like element in a finite difference scheme [7–9], and bar element or shell element in a finite element scheme [10–15]. In order to take into account stresses and associated contact algorithm in the yarn thickness, Rao [16] adopted orthotropic brick element to build a fabric structure at the yarn level. Chocron et al [17–19] further developed the brick element approach in full fabric target simulations in which wave propagation properties and fiber damages under ballistic impact were well validated.

In fabric-reinforced composite materials, a representative element that includes fibers and matric materials is commonly applied for full-scale target simulations. Its properties may derive from small-scale simulation, theoretical model and experimental tests [18,20,21]. In the work of Hayhurst et al. [6], a constitutive model for Kevlar-fabric reinforced epoxy composite was calibrated based on a series of planar impact tests and a large number of quasi-static compressive and tensile tests. It was then implemented in AUTODYN Hydrodynamics by Clegg, Riedel et al. [22,23]. When a significant mismatch in acoustic impedances exists, between fiber and matric materials, challenges in

* Corresponding author.
*E-mail address:* song_stanley@sina.com (Z. Song).

https://doi.org/10.1016/j.ijimpeng.2020.103586
Received 19 September 2019; Received in revised form 25 March 2020; Accepted 6 April 2020
Available online 13 May 2020

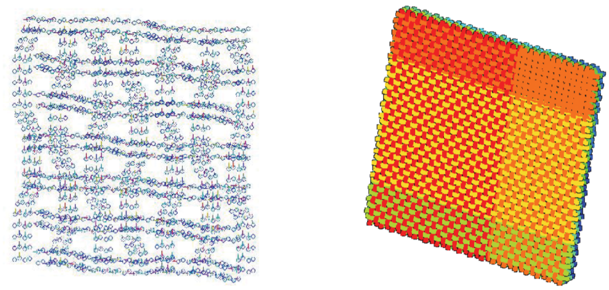

(a) Arrayed SPH particles using MATLAB (b) Generated plain weavein AUTODYN

**Fig. 1.** Construction of the SPH-based fabric model in plain weave.

integrating the governing equations are expected. At extremely high strain rates, the fibers and matrix materials would have dissimilar characteristic times for wave propagations and equilibration. Hence, the composite would not behave as a homogenized material based on a representative cell consisting of fiber and matrix materials. To overcome this limitation, Alexander et al. [24] rebuilt periodically arrayed carbon fibers within an epoxy matrix using the Euler solver CTH, and investigated the propagation of shock waves inside the composite under one-dimensional planar impact. Chocrona et al [18] developed the meso-scale computational model in which the yarn, matrix and interfacial materials are built separately using brick finite elements based on given geometry. It provides a feasible way to analyze the dynamic response of composite materials and determine properly the material properties from experimental tests such as Hopkinson bar compression, shock compression and ballistic tests.

In a Whipple shield against HVI, the fragmentation of a bumper layer and/or a stuffed layer is one of key features of a collision event. It is still difficult in a HVI test to quantitatively evaluate the performance of a fiber fabric, serving as the filler layer of a Whipple. Difficulties also arise in numerical simulations when tracking the spreading of formed debris using either Lagrangian algorithm or Euler algorithm. Exclusive of the implicit uncertainty of numerical accuracy, the meshless algorithms [25–27] provide an efficient approach to handle large deformation and fragmentation. In this work, the computational fabric model is built by SPH particles at the yarn level. The projectile retardation and debris spreading feature are therefore well compared among fabrics with varying fiber properties, woven types, and layouts under simulated conditions of a HVI event. The SPH-based fabric model is augmented for FRP in which the fabric and matrix materials are built according to their geometry. Strictly speaking, the interface effect is not well taken into account considering that the SPH algorithm adopted has only one-order precision. The interfacial strength is negligibly small relative to the developed shock pressure under HVI. Heterogeneity of deformation and damage emerges directly from the fiber and matric material responses. Using this approach with known fiber and epoxy mechanical properties, the computed shock response and damage of a FRP-sandwiched laminate agrees with our previous HVI experimental measurements [28]. The computational model is applied to optimize a hybrid laminate consisting of Kevlar fabric, FRP, and a corrugated alloy plate.

The computational model at yarn level has offered a rapid tool for experimental data analyses and for bridging meso- and macro-scale models towards better understanding of the constitutive behavior of composite materials [6,17,20]. Nonetheless, particular treatment of interfacial SPH particles is still needed, as is well done by Chocron et al [19] in their finite element model, for extending current FRC model to medium strain-rate as demonstrated by experiments [29,30], in which interfacial interaction between fibers and polymers would take place at relatively low impact speeds in the range of 200 m/s to 1200 m/s.

## 2. Modeling fiber fabrics by SPH particles

Advanced fibers, such as carbon fibers, Nextel, and Kevlar, are normally employed in fabric form. The SPH method has the advantages of conveniently rebuilding a fabric with SPH particles alongside a fiber or a yarn, and of bearing large deformation and fragmentation in a HVI process. In this work, modeling and HVI simulations of the fabrics, with various weave patterns, are carried out by using AUTODYN Hydrodynamics.

For a periodically arrayed fabric, the SPH-based model is built by the following operations:

- construct the geometrical equations of each fiber or yarn within the fabric in MATLAB,
- locate repeatedly the SPH particles with given smooth distance alongside each fiber or yarn, and generate an output file that contains particle coordinates and local axial directions of the fiber or yarn,
- input the file into AUTODYN using its EXEDIT module, and generate the SPH model.

In this work, the smooth distance is set to be one and a half SPH particle diameter. The plain weave fabric is discretized by SPH particles alongside each yarn, as shown in Fig. 1(a), having four SPH particles within its cross section. The axial directions of each yarn are also recorded so that orthotropic constitutive relations can be applied. Fig. 1(b) displays the rebuilt fabric in AUTODYN. Following the same operation, the computational models for orthogonally-arranged parallel fibers, twill weave fabric, and three-dimensional orthogonal weave fabric are built in Fig. 2(a), 2(b) and 2(c) respectively.

A laminate composed of randomly oriented fibers, Fig. 2(d), is built by the following operation:

- discretize the laminate by the smooth distance into equally-sized boxes, and compute the total number N of SPH particles based on the fiber volume fraction;
- start a fiber from an open box on a random surface, and run in a random direction to the next open box until it reaches a free surface or ends in an occupied box;
- fill repeatedly new fibers with SPH particles until the number N (starting a fiber from an inner box once surface boxes are all occupied).

In a HVI process, fragmentations will prevail under the interactions of release waves. One approach is that once the computed stress is greater than the material tensile strength, the stresses are automatically zeroed and the failed SPH particle is removed. Note that such scheme may lead to accumulation of errors in system energy given that the elastic energy carried by fractured particles would be artificially removed. Since the SPH algorithm only has one order precision, i.e., one

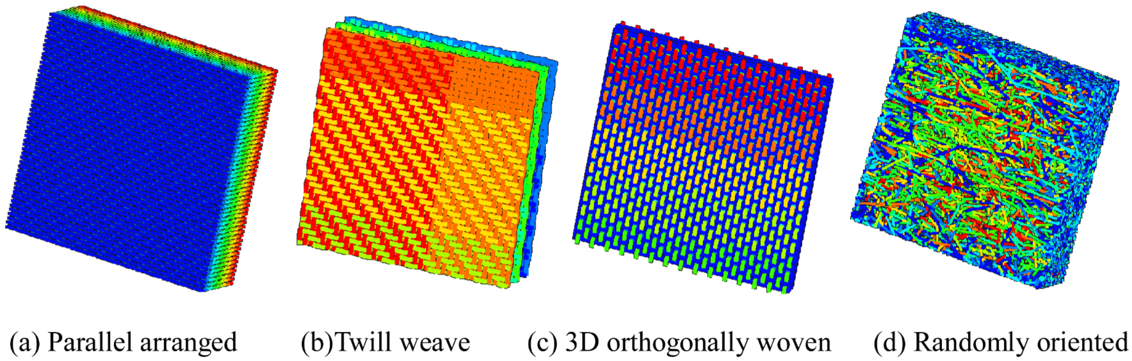


**Fig. 2.** SPH-based fabrics with various patterns.

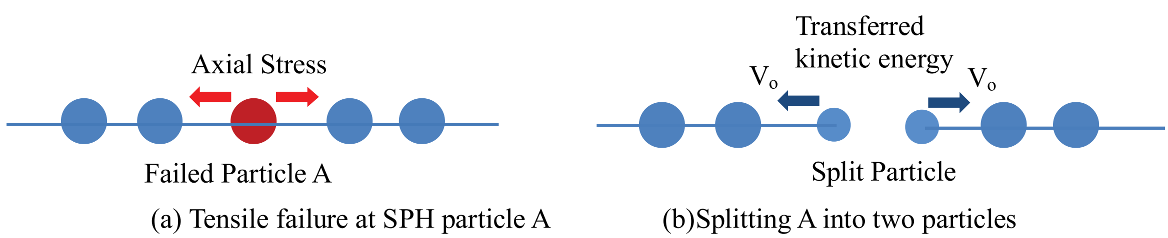


**Fig. 3.** Schematic of the splitting algorithm for SPH particles subjected to tensile damage.

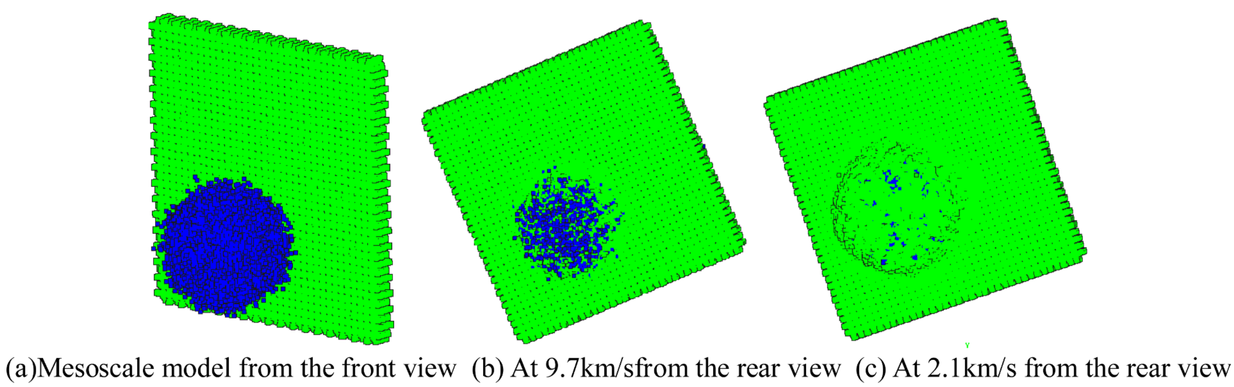


**Fig. 4.** Material distribution of Nextel 610 fabric in plain weave under HVI of a micro aluminum sphere at 9.7 km/s and 2.1 km/s.

SPH particle carries both the velocity and the mass, our modeling of failure is done as follows:

- once the axial stress of a SPH particle attains the failure strength, divide the particle into two (as shown in Fig. 3) carrying the same velocity, temperature and other state variables, but half the mass;
- transfer the stored elastic energy to kinetic energy and add it to newly-formed split particles, next compute associated temperature rise owing to the fracture;
- set the stresses of the split particles to be zero, and ensure both particles could not bear tensile stress in the following computations.

## 3. Evaluating the shielding performance of fabrics under HVI

In a shield against HVI, the selections of the fiber and woven pattern for the laminate layers will depend on the impact condition such as the mass, shape, and projectile velocity. Experimentally, it is still difficult to establish a direct scheme for quantitatively assessing the shielding performance of the filler fabric. Here we resort to SPH simulations to investigate performance of fabrics, serving as multilayers in a stuffed Whipple or a multi-shock Whipple shield [1].

For the fabric subjected to HVI, the interaction among fibers, including compression and sliding between each other, poses a challenge to current meshfree methods. In the optimal transportation meshfree (OTM) method [31], an additional set of geometrical nodes is adopted to interpolate the local deformation field of the second-order precision. It theoretically enables the accurate description of boundaries and their interactions. However, enormous efforts are still required in the OTM method for fulfilling the contact algorithm for fiber fabric involving deformation and fracture. In this work, the interaction force between fibers is computed directly from the distance of adjacent SPH particles, having only the first-order computational precision without the interpolation of local strain gradient field. That is, the nonlinear surface-surface interaction between fibers is simplified to discretized particle-particle interaction which fulfills the efficient and stable simulations but at the loss of computational precision.

Once a projectile impacts the bumper of a Whipple shield, it will produce a debris cloud consisting primarily of micro particulates. The dynamic behavior of the fabrics, when subjected to HVI of the micro particulate is analyzed in what follows.

As shown in Fig. 4(a), the laminate consists of tripled Nextel 610 fabrics of ceramic dioxide fibers in plain weave. The fiber has a diameter of 8μm, and the total thickness of the laminate is therefore 72μm due to the braid structure. As described in Fig. 1, four SPH particles are adopted in the cross section of a fiber, leading to about 125,000 SPH particles in the computational model. The ceramic dioxide fiber has a tensile strength of 2.8 GPa and a tensile modulus of 370 GPa. The instantaneous damage of the fibers is revealed when an aluminum sphere impacts the fabric at velocities of 9.7 km/s and 2.1 km/s, respectively (Fig. 4b,c). At the higher velocity of 9.7 km/s, the sphere particles, represented in blue, immediately penetrate through the laminate in green, leading to total fragmentations of the fibers in the impacted zone, Fig. 4(b).

In such HVI event, a debris cloud will be formed consisting of fragmented fibers and the projectile with varying flying speeds and at scattering angles. The mass distributions of the fragments versus the speed and scattering angle are analyzed for assessing the performance of the filler fabric.

The traditional failure model may not only produce a systematic error in energy, but result in improper spreading of the fragmented fibers. The adoption of the splitting algorithm for fragmented fibers, as described in Fig. 3, is first surveyed by comparing the statistical distributions of the formed fragments with those of the AUTODYN-embedded failure model where the stresses of a failed SPH particle would be artificially removed. The statistical distributions versus the speed and scattering angle both display a few difference between the two failure models at the impact velocity of 9.7 km/s, see Figs. 5(a) and 5(b). Considerable difference is found when the impact velocity is 4.5 km/s, Fig. 6, as the ratio of stored elastic energy of the impacted fabric to the kinetic energy of the sphere grows. The speeds of the formed fragmentations appear to be randomly distributed, depending on the adopted damage model and the fabric texture. Note that the computational results in this work are repeatable. Even though there exist unavoidably bad SPH particles at extremely high speed especially when exceeding 9 km/s, the outcome of the statistical distributions and the free-surface velocity profile as shown in what follows would remain unchanged.

### 3.1. Selection of fibers

Light-weight alloys are normally employed in the bumper material in a Whipple shield. A comparison of the performances of the 2024 aluminum alloy sheet and the Nextel fabric laminate, both having the same areal density, is displayed in Figs. 7 and 8. For a 9.7 km/s impact, the mass distribution of the Nextel fragments shows three typical peaks in the speed range from 5 km/s to 9 km/s, with the maximum at 7.5 km/s, see Fig. 7(a). Compared with the 2024 alloy sheet, the Nextel fabric is capable of absorbing more kinetic energy with less high-speed fragments exceeding 7.6 km/s, and with more low-speed fragments below 3.5 km/s. The formed Nextel fabric fragments are mainly concentrated at small scattering angles, below 10° in Figure 7(b), with the 2024 alloy fragments showing a different distribution. Analogous to the HVI condition, at a relatively low impact velocity of 2.1 km/s, the Nextel fabric exhibits a better retardation effect but worse spreading of the formed fragments (in Figs. 8).

In a homogeneous metallic sheet, strong shock waves, 3D in nature, will form under a sphere impact and lead to wide spreading of the induced debris cloud. By contrast, the fabric laminate has equivalently low acoustic impedance along the thickness. It is first compressed and then deformed while absorbing more kinetic energy due to its higher strength. The lightweight alloy and fiber fabric are therefore preferable, respectively, to the bumper sheet and the filler layer in an enhanced Whipple shield.

The effect of the fiber strength is illustrated in Figs. 9 and 10 assuming that the ceramic dioxide fibers have the same elastic modulus but varying tensile strengths of 2.8 GPa and 5.0 GPa. At an impact velocity of 9.7 km/s, multiple failure sites result in massive fragmentation of the impacted fibers. A slight difference between fibers with varying strengths is observed from the statistical histograms of speed, Fig. 9(a), and scattering angle, Fig. 9(b). At a low impact velocity, however, the fabric made up of high-strength fibers is capable of absorbing more kinetic energy and generating a wider distribution of angular scattering of the debris cloud, see Figs. 10.

The performance of carbon fibers made from TORAY Inc. is summarized in Figs. 11 to 13. In Table 1 fiber properties are reported. The carbon fiber T300 has the smallest tensile modulus of 231 GPa while the fiber T1000 has the highest tensile strength of 7.02 GPa. The graphite fiber M60JB has the highest tensile modulus of 590 GPa. For plain weave fabrics, the fibers that have higher strength would produce less fragments in the high speed range, while the fibers that have higher tensile modulus would form a debris cloud with a more flattened distribution versus the speed. At an impact velocity of 9.7 km/s, there exists a conspicuous peak in the distribution at the speed of 5.6 km/s both for the low-modulus fibers T300 and T1000, Fig. 11. The fiber

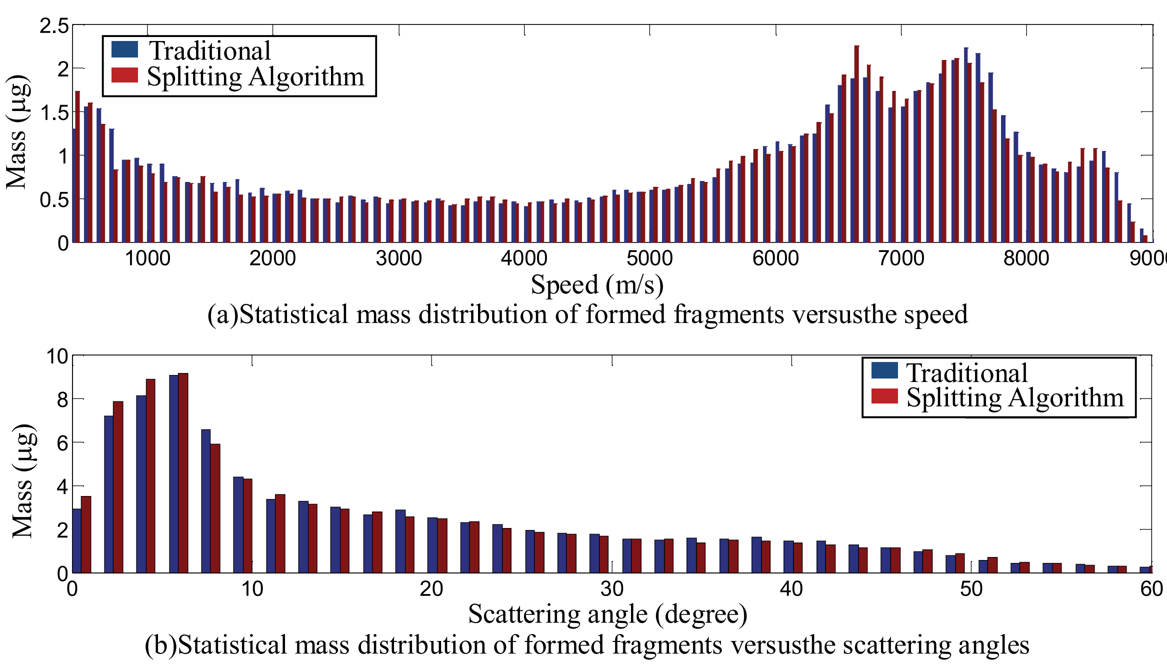


(a)Statistical mass distribution of formed fragments versusthe speed

(b)Statistical mass distribution of formed fragments versusthe scattering angles

**Fig. 5.** Comparison between damage model for Nextel plain weave fabric under a sphere impact at 9.7 km/s.

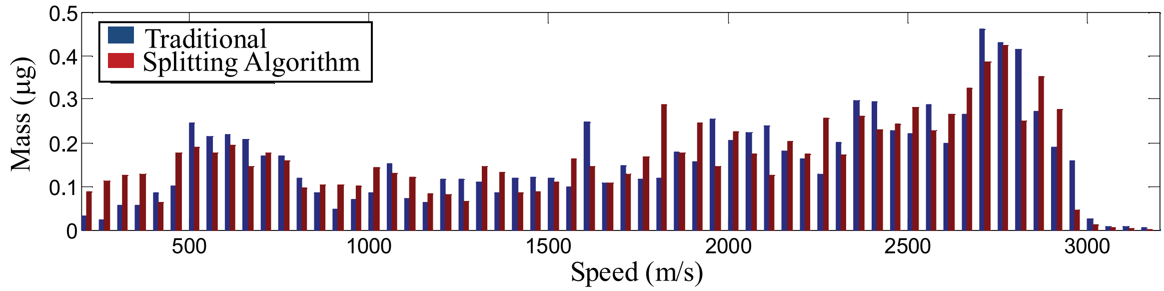


**Fig. 6.** Comparison between damage models for Nextel plain weave fabric under a sphere impact at 4.5 km/s.

T1000 produces fewer fragments in the high speed range (Fig. 11(b)) because of its much higher tensile strength of 7.02 GPa as compared with M60JB, which strength is 3.94 GPa.

The damages of the plain weave fabrics are revealed in Figs. 12 under a sphere impact of 2.1 km/s. For the M60JB fabric, Fig. 12(b), the formed shock wave propagates at a faster speed due to their higher modulus, and the fibers fragment into smaller particulates mainly due to their lower strength as compared with the fibers T1000. As illustrated in Fig. 13, the T1000 fabric forms more low speed fragments than the M60JB fabric. The mass-weighted average speed of formed fragments is 785 m/s for T1000 fibers, much lower than that of 929m/s for M60JB fibers. Hence, at a low impact velocity, the high strength fibers have the great stopping or low projectile residual velocity.

### 3.2. *Influence of woven patterns*

Impact experiments performed in the range of 2-3 km/s have demonstrated that 3D woven SiC fabric sheets [29] have better shielding performance than their 2D counterpart does. In a bumper and/or stuffed layer of a Whipple, however, the fabric layer is much thinner than that used in [29], and would undergo fragmentation even under a medium impact of 2-3 km/s. The 3D orthogonally woven fabric shown in Fig. 2(c), when impact at velocities of 9.7 km/s and 2.1 km/s, did not exhibit advantages of kinetic energy absorption and formation of a widely-spread cloud of fragments. As displayed in Fig. 14, at 9.7 km/s, the 2D plain weave and 3D orthogonally-woven fabrics have similar fragment speed and angular distributions. At a lower velocity of 2.1 km/s, the 3D fabric produces more low-speed fragments, ranging from 200 m/s to 400 m/s, but also results in high-speed fragments ranging from 1700 m/s to 1850 m/s, see Fig. 15. This explains the reason why the Nextel fabric, in 2D woven pattern, still has wide applicability in Whipple shields.

To examine the effect of in-plane weaving pattern on performance against HVI, we consider the plain weave and the twill weave shown Fig. 16, the latter of which forms fewer yarn intersections as shown in Fig. 2(b). At an impact velocity of 9.7 km/s, the peak of the fragment distribution versus speed occurs at 7.7 km/s for the twill weave, while for the plain weave it occurs at 7.4 km/s. Hence, the plain weave has the advantage of retarding the sphere impact owing to the formation of more intersections, equivalent to more out-of-plane components of the yarns along the shock direction.

The fragmentation features of the plain weave, parallel-arranged fibers, and randomly oriented fibers are displayed in Figs. 17. It is found that the sheet made from randomly-oriented fibers has the highest mass distribution in the high-speed range from 7.4 km/s to 9 km/s at a HVI of 9.7 km/s, revealing the worst shielding performance among the three patterns. The sheet made from parallel-arranged fibers has the least fragments in the speeds above 7.4 km/s, but forms a high peak at 7 km/s. The plain weave fabric produces the largest number of fragments, in the low-speed range, due to constraints at yarns intersections. Among the three patterns, the difference in the distribution of the scattering angle is relatively small.

Simulation results of the HVI process at an impact velocity 9.7 km/s, for the tri-layered fabric equidistantly placed with a standoff of 24 μm, are reported in Figs. 18. Compared with the plain weave in compact form, more fragments are formed for the equidistant layout due to the multiple shock processes. The mass-weighted average speeds of formed fragments are 5700 m/s and 4800 m/s for the compact fabric sheet and

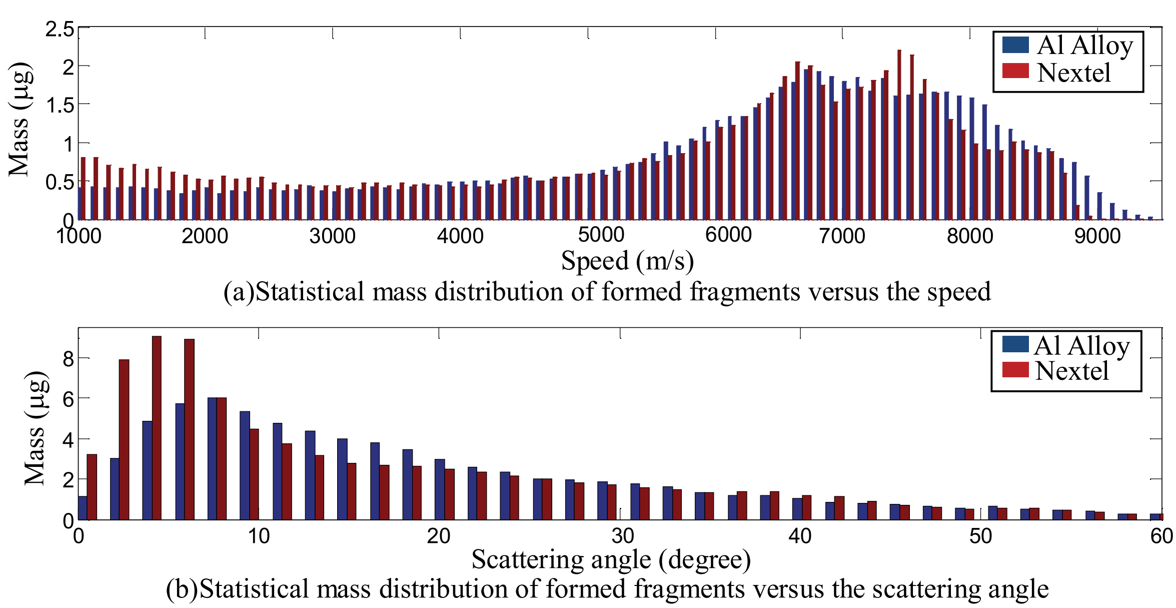


**Fig. 7.** Comparison between 2024 aluminum alloy sheet and Nextel fabric laminate under a sphere impact at 9.7 km/s.

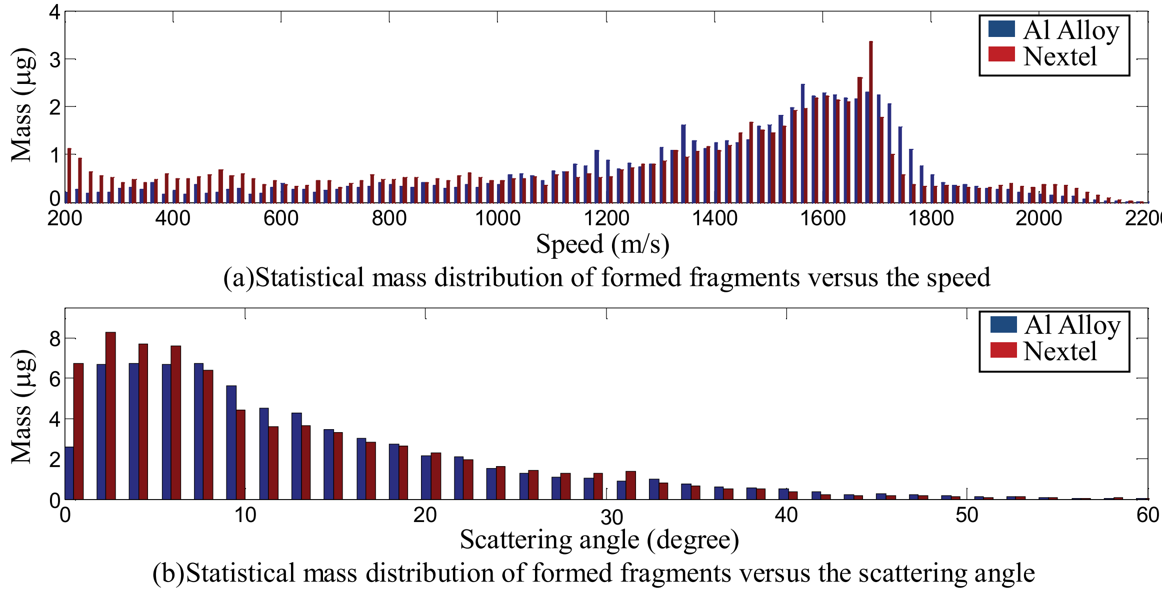


(a)Statistical mass distribution of formed fragments versus the speed

(b)Statistical mass distribution of formed fragments versus the scattering angle

**Fig. 8.** Comparison between 2024 aluminum alloy sheet and Nextel fabric laminate under a sphere impact at 2.1 km/s.

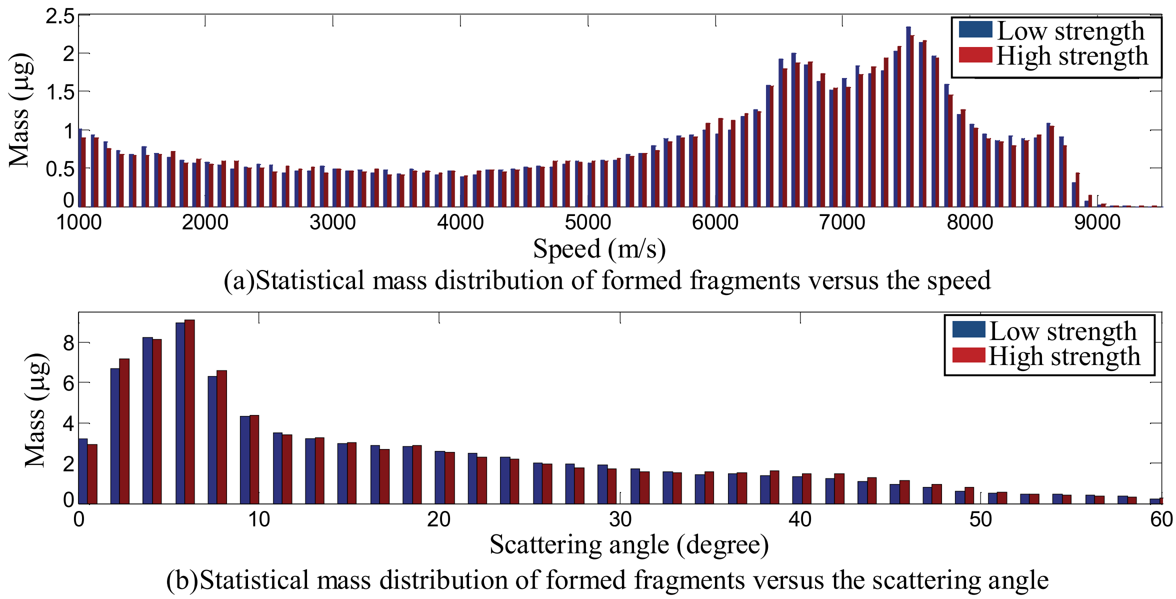


(a)Statistical mass distribution of formed fragments versus the speed

(b)Statistical mass distribution of formed fragments versus the scattering angle

**Fig. 9.** Comparison between fabrics with various tensile strengths under a sphere impact at 9.7 km/s.

equidistant fabric sheet, respectively. The equidistant layout has the better performance in retarding a hypervelocity projectile, although there are more fragments at the hyper-speeds of about 8.7 km/s. As displayed in Fig. 18(b), the extra amount of fragments formed from the equidistant layout is distributed in a large scattering angle range.

### 3.3. Influence of pre-compression

The debris cloud resulting from projectile/bumper impact may consist of congregated fragments and micro dust formed by micro-jets and micro-spalled particulates, as well as vaporized gas in events at an extremely high impact speed. It is known from planar impact tests that micro-jets would be formed and eject from concaves and/or grooves of the target surface, having the speed about 1.1-1.2 times that of the micro-spalled fragments [32]. The formed debris cloud in a HVI process, poses a great modeling challenge in view of the spanned size-scales from sub-micro to millimeter. In this work, particular treatment is given for the micro dust that would pre-compress the filler fabric as a continually applied boundary force prior to the arrival of congregated or large fragments. As shown in Fig. 19, the micro dust ejects from the impact point A of the bumper, and expands in linear distributions of velocity and density in terms of:

$$v(\bar{r}) = v_o + (v_1 - v_o)\cdot\bar{r};\ \rho(\bar{r}) = \rho_o(1 - \bar{r}) \tag{1}$$

in which $\bar{r} = (r - r_b)/(r_a - r_b)$ is the normalized distance. The radii $r_a$ and $r_b$ represent the leading and back edges of the micro dust, travelling with the speeds $v_1$ and $v_o$, respectively. In this work, we set the front-edge speed $v_1$ to be $1.2v_o$ with $v_o$ also being the speed of a macro fragment as shown in Fig. 19. The mass of the micro dust that impacts the filler layer is

$$M_{dust} = \rho_o \int_{r_b}^{r_a} r^2(1 - \bar{r})dr\cdot\delta\theta \tag{2}$$

The density $\rho_o$ can therefore be determined by prescribing $M_{dust}$.

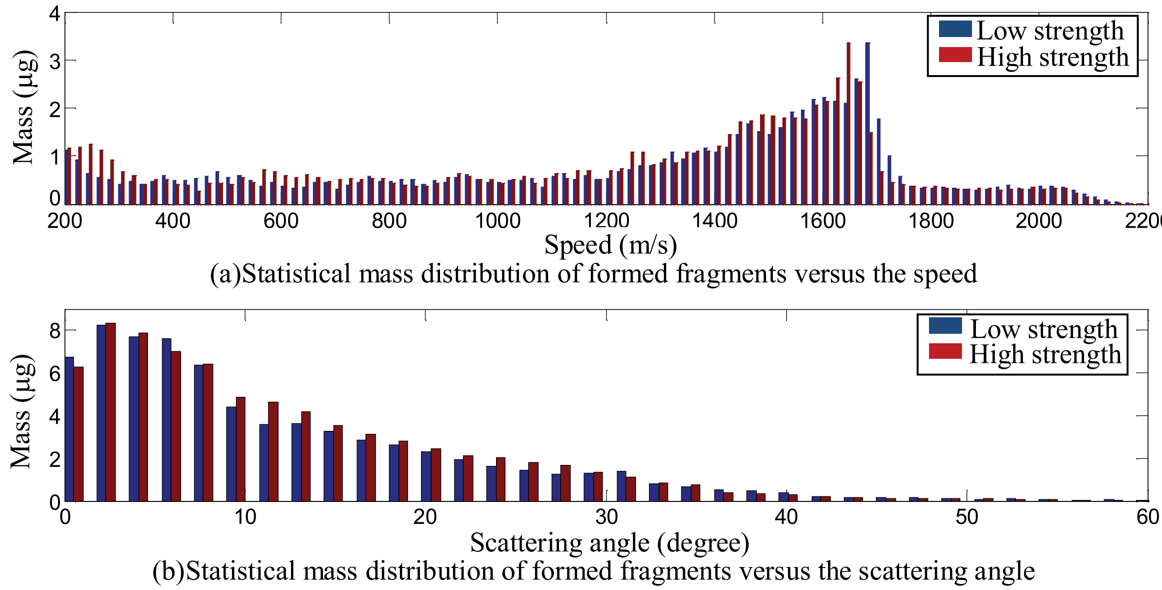


**Fig. 10.** Comparison between fabrics with various tensile strengths under a sphere impact at 2.1 km/s.

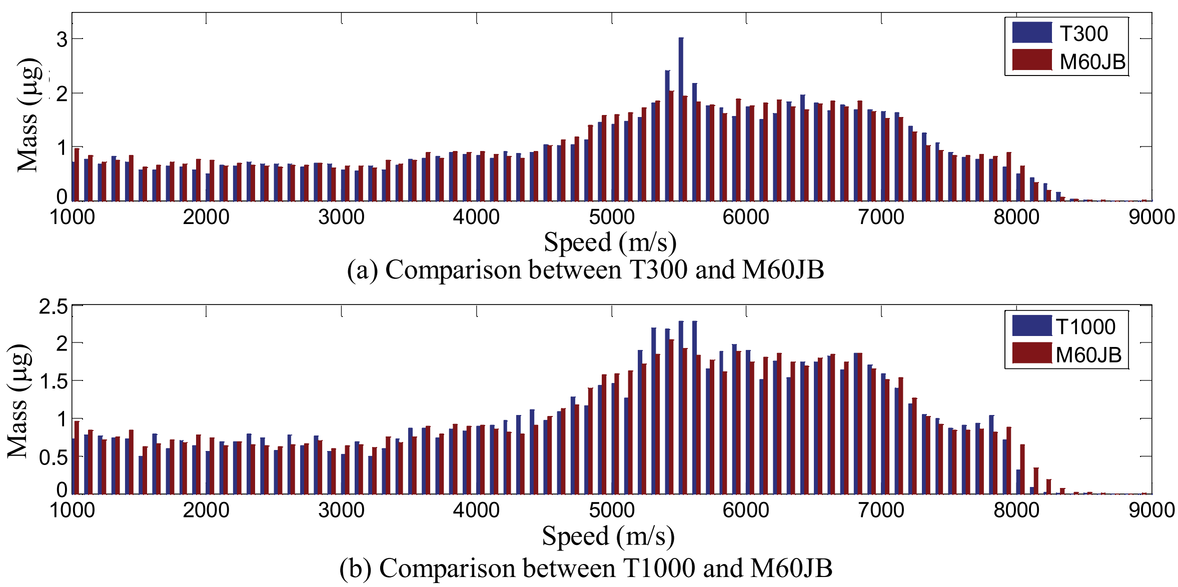


**Fig. 11.** Mass distribution of the formed fragments versus the speed under sphere impact at 9.7 km/s.

**Table 1**
Mechanical properties of TORAY carbon fibers.

| Fiber model | Density (g/cm$^3$) | Tensile strength (GPa) | Tensile modulus (GPa) |
|---|---|---|---|
| T300 | 1.76 | 3.54 | 231 |
| T1000 | 1.80 | 7.02 | 296 |
| M60JB | 1.95 | 3.94 | 590 |

The volume of the dust that arrives and interacts with an outmost SPH particle of the filler layer at the time increment [$t_n$, $t_{n+1}$] can be computed from

$$V_{dust} = \pi R_{sph}^2(\bar{r}^n - \bar{r}^{n+1})(r_a^{n+1} - r_b^{n+1}) \tag{3}$$

where $\pi R_{sph}^2$ is the swept area of the SPH particle, $\bar{r}^n$ and $\bar{r}^{n+1}$ are the normalized radii of the SPH particle at the time $t_n$ and $t_{n+1}$, respectively, and $r_a^{n+1}$ and $r_b^{n+1}$ are the radii of front and back edges of the micro dust respectively. The continuous boundary force is thus applied with the assumption that the arriving dust, with a momentum

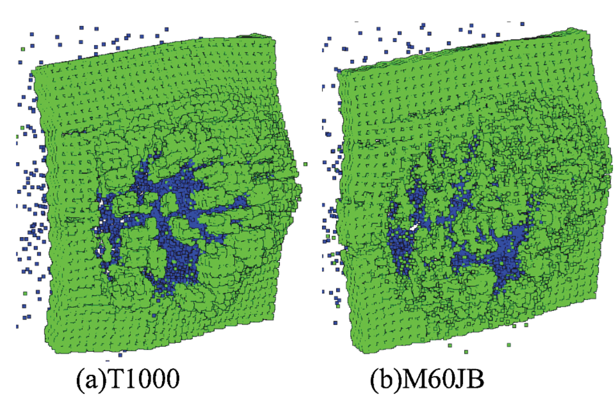


**Fig. 12.** The instantaneous material configurations of the plain weave fabrics made up of TORAY T1000 and M60JB fibers respectively under a sphere impact at 2.1 km/s.

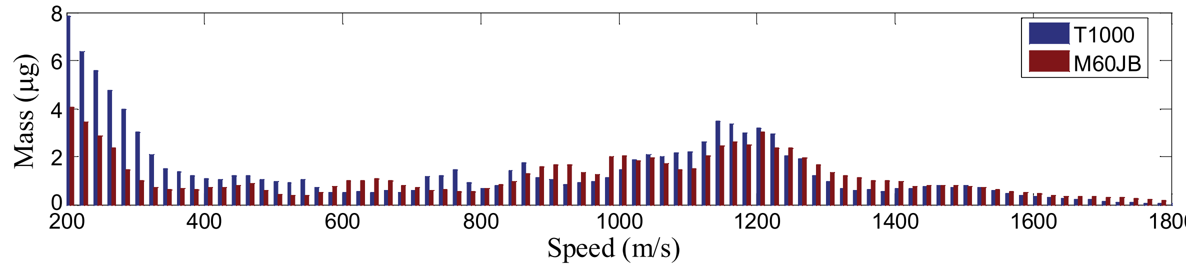


**Fig. 13.** Mass distribution of the formed fragments versus the speed under a sphere impact at 2.1 km/s.

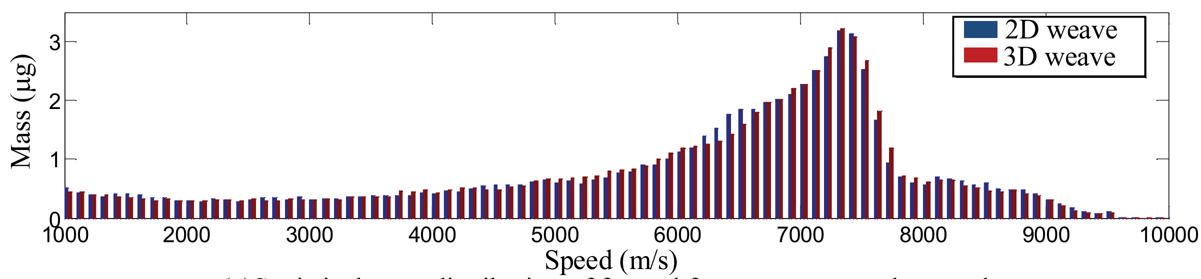


(a)Statistical mass distribution of formed fragments versus the speed

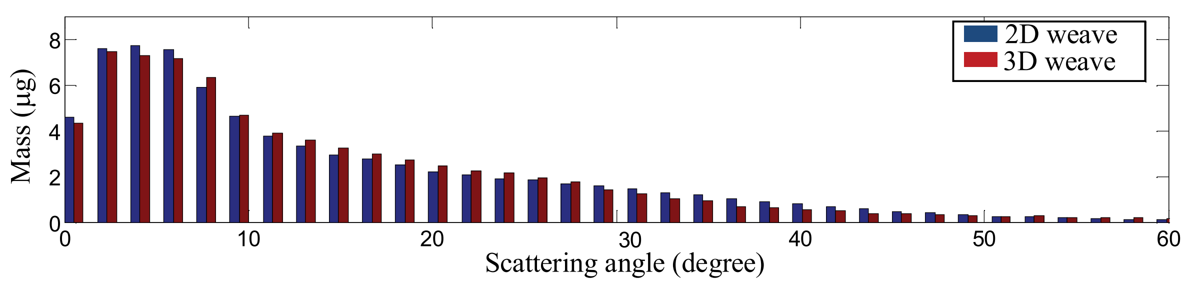


(b)Statistical mass distribution of formed fragments versus scattering angle

**Fig. 14.** Comparison between fabrics with different weaves under a sphere impact at 9.7 km/s.

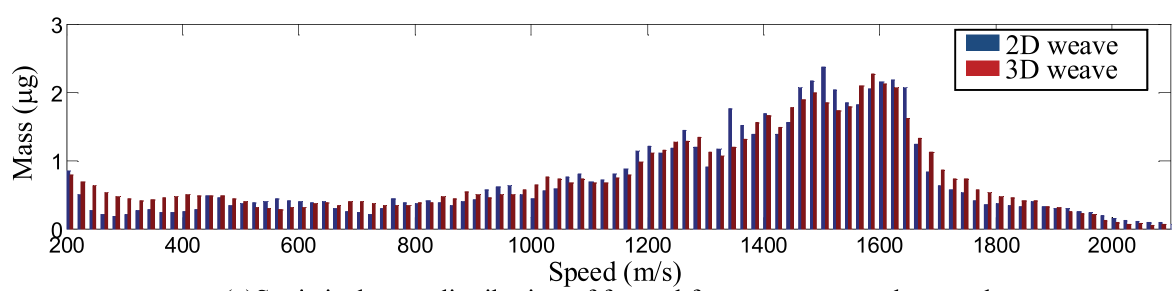


(a)Statistical mass distribution of formed fragments versus the speed

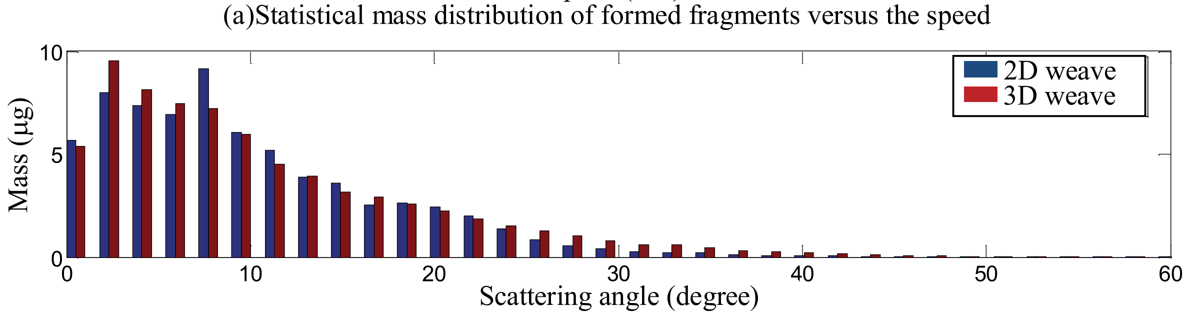


(b)Statistical mass distribution of formed fragments versus scattering angle

**Fig. 15.** Comparison between fabrics with 2D and 3D woven patterns under sphere impact at 2.1 km/s.

$v(\bar{r}^{n+1/2})\rho(\bar{r}^{n+1/2})V_{dust}$, would be adhere to the SPH particle.

The outmost SPH particles of the filler layer, which interact with the micro dust, can be determined in the polar coordinate $(R, \theta, \varphi)$ centered at the impact point A by spatially dividing meshes along $\theta$ and $\varphi$ directions, and then searching the minimal R of the SPH particles in every mesh $(\theta_i, \varphi_i)$ at each time step.

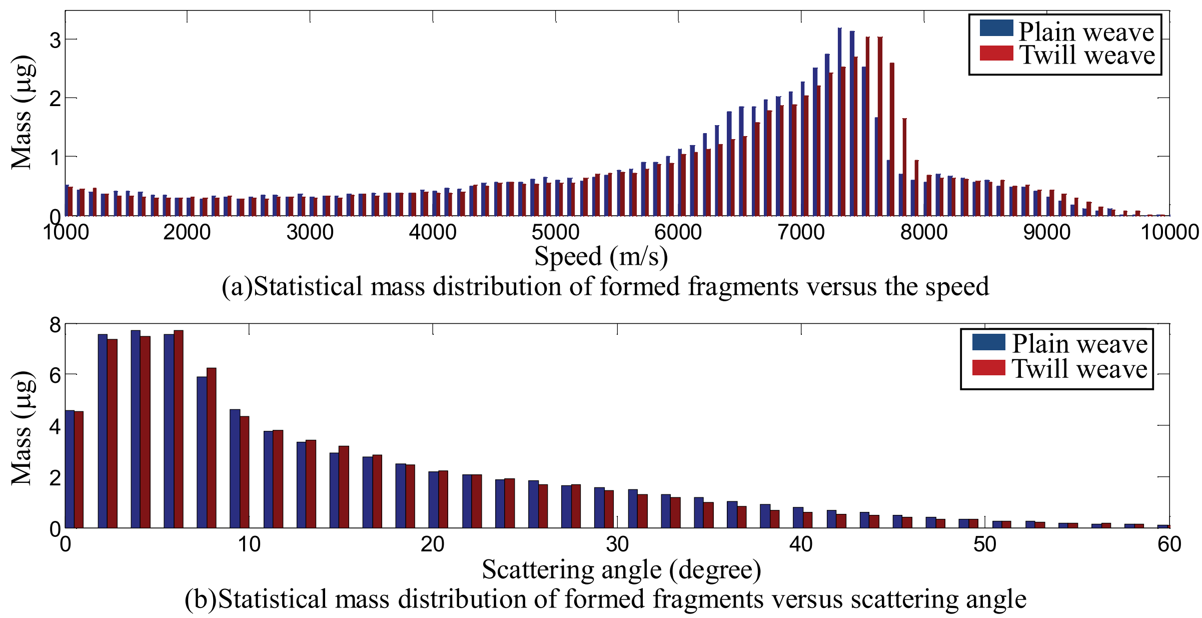


**Fig. 16.** Comparison between the plain weave and the twill weave under a sphere impact at 9.7 km/s.

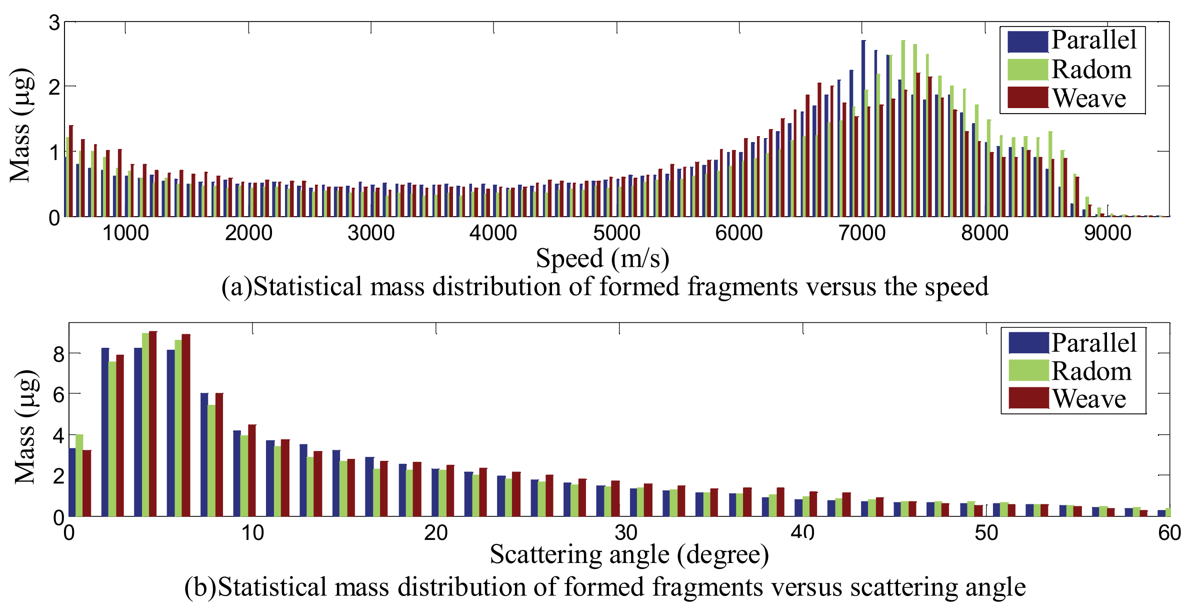


**Fig. 17.** Comparison among the plain weave, parallel-arranged fibers, and randomly oriented fibers under a sphere impact at 9.7 km/s.

Based on the above computational model for the micro dust, the filler fabric is first pre-compressed by the micro dust as shown in Fig. 20, and then deforms and fragments under HVI of an aluminum sphere at 9.7 km/s. Since the applied micro dust has one tenth of the mass of the sphere, it accelerates the pre-compressed fabric to about 500 m/s, as illustrated by the peak shift from 7000 m/s to 7500 m/s (Fig. 21(a)) for parallel-arranged fibers, and from 7300 m/s to 8000 m/s (Fig. 21(b)) for randomly oriented fibers. Moreover, the pre-compression of the fabric significantly heightens the peak of the speed distribution. It is particularly disadvantageous for randomly-oriented fibers in which more hypervelocity fragments are formed ranging from 7600 m/s through 8300 m/s and above 8500 m/s.

## 4. Shock compression and damage of FRP composites

FRP composites are normally treated as continuous and homogenized materials in numerical simulations. The assumption applies to quasi-static and medium strain-rate conditions where the reinforced fibers, the matrix material and their interfaces would behave harmoniously as a whole. In a planar impact experiment, however, the carbon fiber fabrics keep their integrity, while the epoxy resin totally disintegrates as shown in Fig. 22. It therefore is debatable as to whether fibers and polymer matrix can be treated as homogenized elements of the modeled FRP composite at high strain-rate loading.

### *4.1. Computational model for FRP composites*

Regardless of material damage, fibers and matrix materials normally have different characteristic times for shock waves to propagate and equilibrate in view of the mismatch of acoustic impedances between them. To reproduce the wave propagation and subsequent deformation and damage in FRP composites, a modeling attempt is made in this work by building the fabric and the polymer separately. In Fig. 23, we first build the fabric by SPH particles based on the texture of

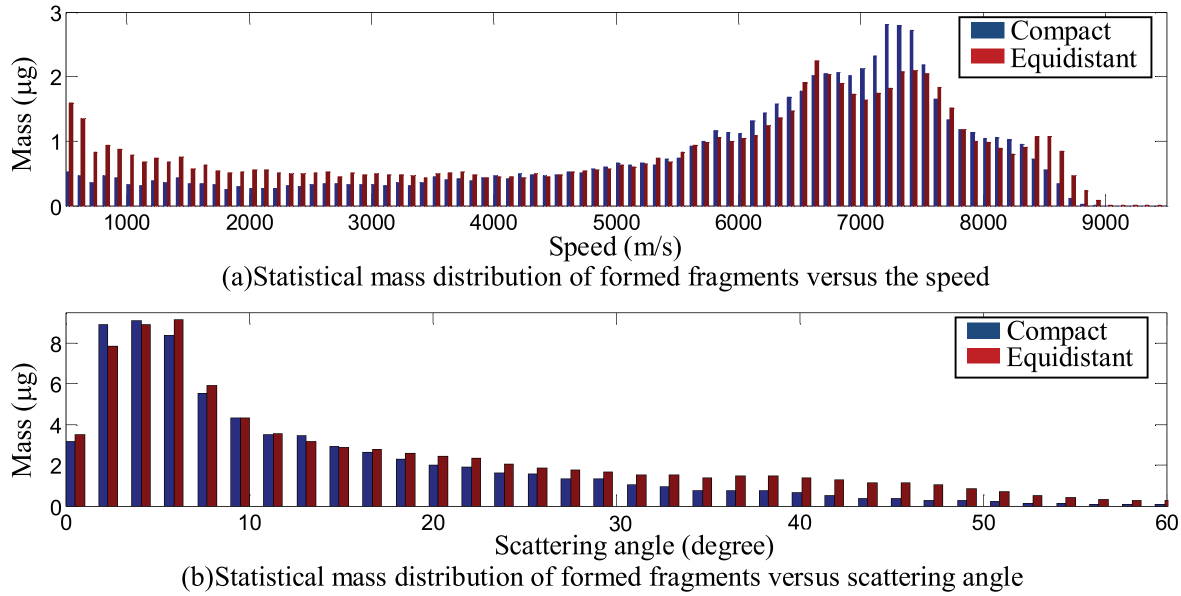


**Fig. 18.** Comparison between fabrics in compact form and equidistant layout at an impact velocity 9.7 km/s.

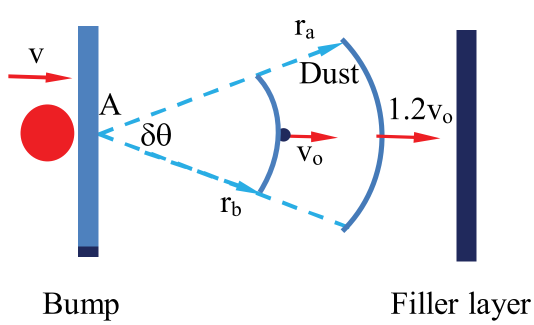


**Fig. 19.** The schematic diagram of the micro dust formed from projectile/bumper impact.

the concerned FRP sample, and then fill the sample with SPH particles of the epoxy resin.

The nonhomogeneous and anisotropic behavior of the FRP composite, including the elastoplastic properties and the damage criteria, are thus determined directly from the reinforced fabric and the matrix materials. Since the fabric is meshed based on the strand yarn rather than the fiber in this macro model, the axial stress and strain of the fiber are assumed to take the form:

$$\sigma_f = \sigma_F/(1-f) \tag{4}$$

$$\varepsilon_f = \varepsilon_F - \delta \tag{5}$$

where the subscripts f and F denote the fiber and the strand yarn, respectively. The concept of initial strain distribution, $\delta$, is herein introduced to describe the asynchronous deformation in the fibers of a strand yarn. Given the macro axial strain $\varepsilon_F$, the increment of the damage variable $f$ that denotes the volume fraction of fractured fibers can be determined from Eq. (5) based on a known tensile criterion.

The constitutive relation for the fabric is thus given by

$$\sigma_F = (\varepsilon_F - \delta)(1-f)E \tag{6}$$

where E is the fiber longitudinal Young's modulus.

Theoretically, we can introduce particular SPH particles on the fiber/polymer interfaces. The description of the interfacial particles, however, still remains open and depends on the knowledge of the polymer meso-structure. Moreover, two-order precision of meshless algorithms are demanded for properly handling the interfacial conditions. In this work, the interfacial effect isn't taken into account under the assumption that the interfacial strength is negligibly small compared with the applied shock pressure.

The validity of the SPH-based CFRE computational model is preliminarily assessed by traditional plate impact test as shown in Fig. 24(a). One fourth of the computation model is built accordingly,

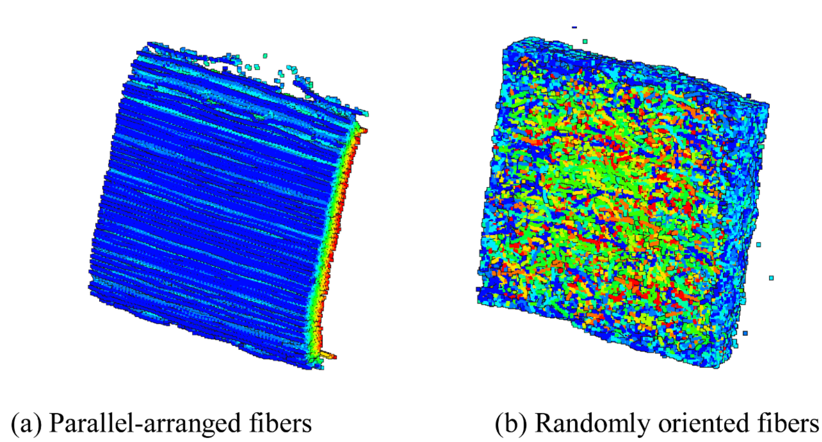


**Fig. 20.** Pre-compression of the fabrics by the micro dust.

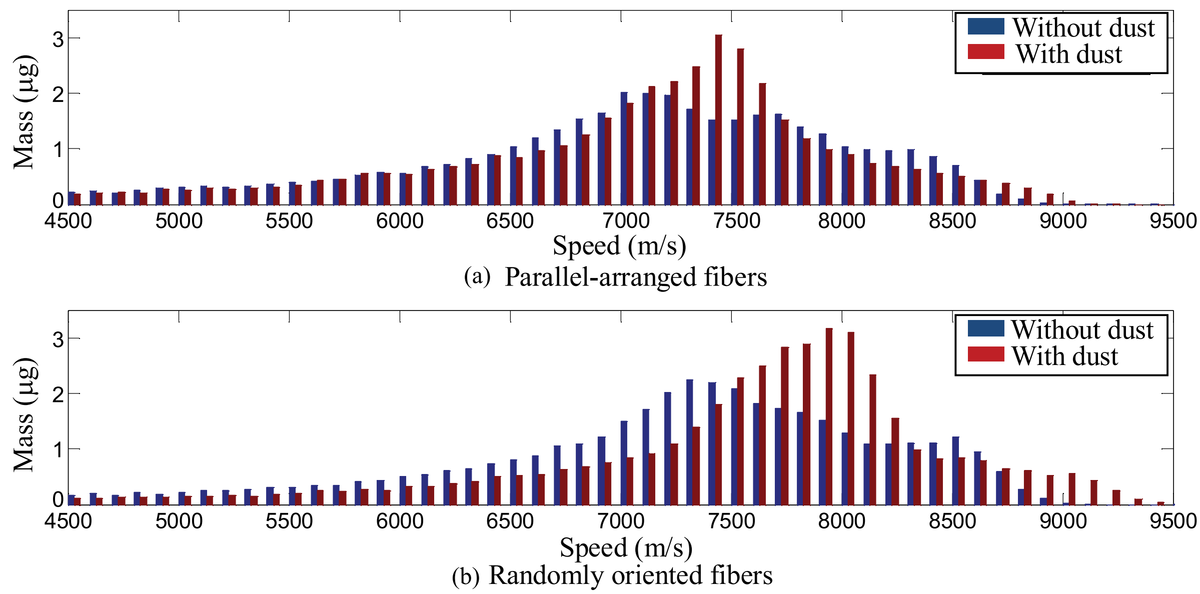


**Fig. 21.** Comparison between computational models with and without micro-dust at sphere impact velocity of 9.7 km/s.

**Fig. 22.** Recovered five-layered carbon-fiber fabrics and epoxy composite sample subjected to an aluminum flyer impact at 327 m/s.

Fig. 24(b), where the flyer, the carbon-fiber fabric reinforced epoxy (CFRE) composite sample, and the LiF window are all meshed into SPH particles. As described in Figs. 23(a), the carbon-fiber fabric is meshed based on the strand yarn with forty SPH particles on its cross section. The constitutive relations for the carbon fiber and the epoxy resin are given separately in which the young's modulus E is 234 GPa for the fiber, and the shear modulus G is 1.6 GPa for the epoxy resin. For damages of the CFRE composite, the fiber has a longitudinal tensile strength of 2.1 GPa and a transverse shear strength of 1.0 GPa, and the epoxy has a shear strength of 100 MPa at high strain rates. Maximum stress criterion of fragile fracture is applied for both fabric and epoxy resin materials. Both the shear modulus and the shear stresses are zeroed once the concerned SPH particle fails.

In planar dynamic compression tests, the interfacial particle velocity profile measured by Doppler interferometer, as shown in Fig. 24(a), contains shock compression and subsequent unloading with material damages. Exclusive of the first slow ramp rise of the velocity due to the employed artificial viscosity for inhibiting numerical oscillation, the computed shock peak approximately accords with the experimental result as shown in Fig. 25. It reveals the feasibility of the applied SPH-based CFRE model as well as the EOS of the materials applied in this work. Without adjusting the damage criteria for the fiber and the epoxy resin, the computed interfacial velocity profile roughly follows the measured curve in the unloading zone. More modeling efforts are needed for accurately reproducing the experimental velocity profile. It would include the accurate characterizations of the sample texture, and the plastic deformation and damage of the epoxy resin. As for the fragmentation of the fabric and/or its composite under HVI, the validation of the simulations needs the experimental measurement of the distribution of the formed debris cloud which is actually a big challenge.

### 4.2. Examples of Alloy/CFRE hybrid laminates

For a single-layered shield resisting a HVI, the lightweight alloy panel produces a spalled film, while the CFRE composite panel undergoes extensive fragile damage during penetration. As revealed by

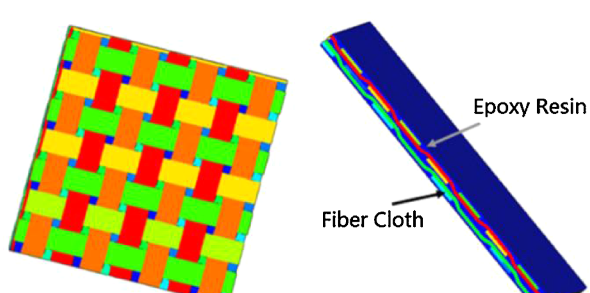


(a)Building offabric based on given texture(b)Filling with matrix material

**Fig. 23.** The construction of the FRP model consisting of fabric and epoxy resin both using SPH particles.

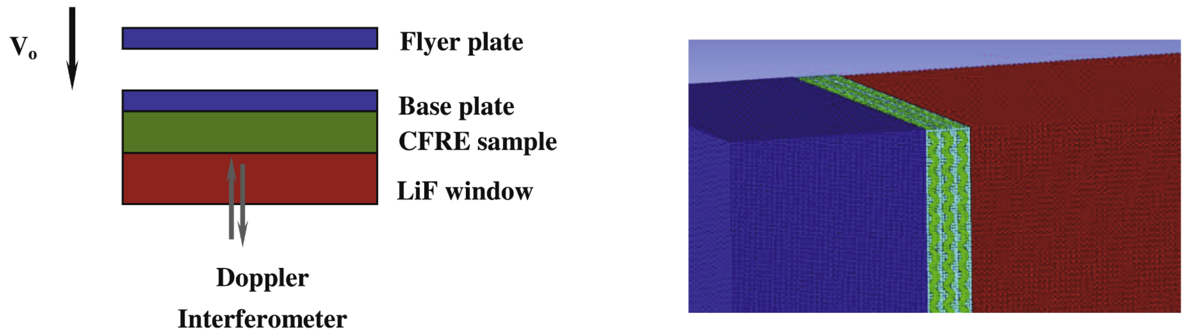


(a) Experimental configuration (b) Computational model

**Fig. 24.** Planar plate impact test on Carbon-fiber fabric reinforced composite sample and its computational model.

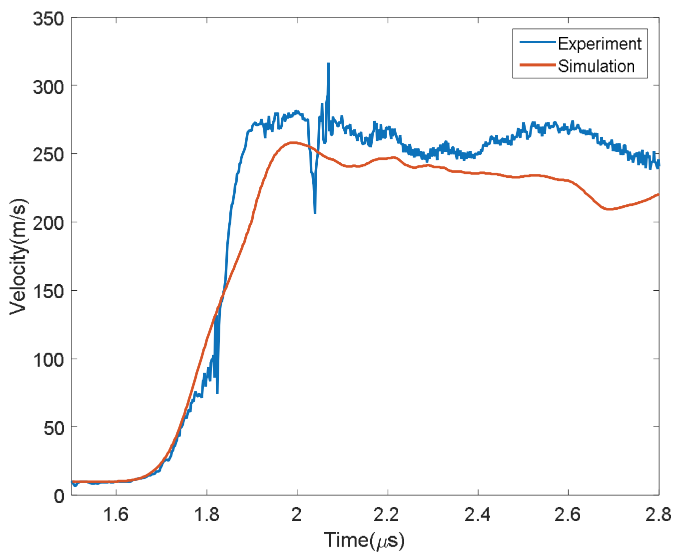


**Fig. 25.** Experimental and computed particle velocities on the CFRE/LiF interface under an aluminum plate impact at 320 m/s.

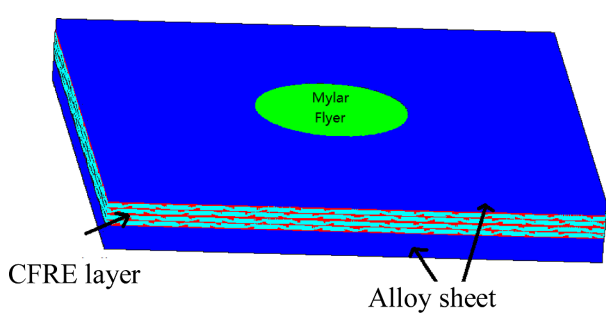


**Fig. 26.** Computational model for the CFRE-sandwiched 2024 alloy laminate labelled by Al/2C/2Al.

previous experiments [10], an aluminum alloy - CFRE hybrid laminate exhibits better performance in attenuating the shocking peak and absorbing the kinetic energy of the impactor.

HVI simulations were carried out for 5.0-mm-thickness hybrid laminates with varying stacking patterns of 2Al/C/2Al, Al/2C/2Al, 2Al/2C/Al, and Al/C/Al/C/Al where Al and C denote 2024 aluminum alloy and CFRE composite, respectively, and the number 2 denotes double the thickness of 1.0 mm. Fig. 26 displays the SPH-based computational model in which the hybrid laminate labelled by Al/2C/2Al is impacted by a 10-mm-diameter and 0.1-mm-thickness Mylar film at 9.0 km/s.

Figs. 27 to 30 display the damage patterns and computed rear-surface velocity profiles for the hybrid laminates with the stacking patterns 2Al/C/2Al, Al/2C/2Al, 2Al/2C/Al, and Al/C/Al/C/Al respectively. In full agreement with previous experiments [10], the shielding performance enhances accordingly from Fig. 27 to Fig. 30 associated with the attenuation of the peak rear-surface velocity profile. The laminate labelled by 2Al/C/2Al that uses only a 1.0 mm thick CFRE layer produces the largest cut-through hole, associated with the highest rear-surface velocity peak. Compared with Al/2C/2Al, the laminate 2Al/2C/Al that uses a 2.0 mm thick alloy panel on the front surface has improved performance with further weakening the shock peak. As is also observed in experiments, the five-layered laminate Al/C/Al/C/Al, which contains two more interfaces, endures the flyer impact without penetration, as shown in Fig. 30.

The shielding performance of a hybrid laminate can be remarkably enhanced by adopting alternative-stacking and multi-layered laminate although its areal density still remains unchanged. In Figs. 28(b) and 30(b), the first peak of the rear-surface velocity drops from 666 m/s for Al/2C/2Al to 500 m/s for Al/C/Al/C/Al, revealing the contribution of the alloy/CRFE interfaces to the efficient reduction of the shock wave from the flyer impact.

The evolutions of the shock pressure along the thickness of the laminates Al/2C/2Al and Al/C/Al/C/Al are shown in Figs. 31(a) and 31(b), respectively. These plots illustrate the effect of the alloy/CRFE interfaces. For both laminates, a short-pulse shock wave would be formed inside the front alloy panel with the magnitude of about 70 GPa when subjected to the Mylar flyer impact at 9 km/s. As the shock wave propagates along the thickness, it decays rapidly because of the presence of unloading waves from the front surface of the flyer film. The shock peak drops to about 6 GPa when it arrives at the first alloy/CRFE interface at about 0.2 μs. In contrast to the Al/2C/2Al case, there is an extra interface at the thickness of 2.0 mm in the Al/C/Al/C/Al case. This leads to the broadening of the shock peak when it travels from the heterogeneous CRFE layer to the alloy panel (having a higher acoustic impedance) at 0.4 μs. At 0.6 μs, the shock peak arrives at the third interface in Al/C/Al/C/Al, and the pressure drops as the acoustic impedance decreases. In Fig. 31(a), the shock peak has been remarkably weakened below 3.0 GPa ahead of the third interface, and then widely dispersed along the thickness ranging from 3.5 mm to 4.5 mm at times from 0.6 μs to 1.2 μs.

It is seen from the simulations that the alloy/CRFE interfaces, being not an ideal mathematical plane, contribute to spreading the shock peak and therefore improving the capability of undergoing large deformation and associated kinetic energy adsorption.

### 4.3. Optimization of the hybrid laminates resisting HVI

For an optimized shield that resists HVI, it should first absorb the shock wave by effectively weakening the shock peak to avoid localized damage such as spallation, and then have the capability of producing large deformation to absorb the residual kinetic energy. As evident in previous simulations, the CFRE layer has been used in the hybrid

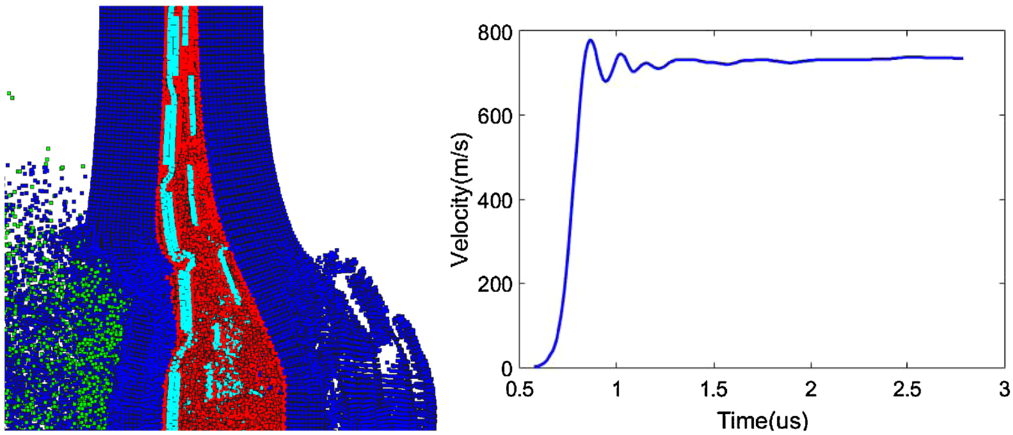


(a) Damage of the impacted sample (b) Particle velocity profile on the rear wall

**Fig. 27.** Simulation results for the hybrid laminate labeled by 2Al/C/2Al.

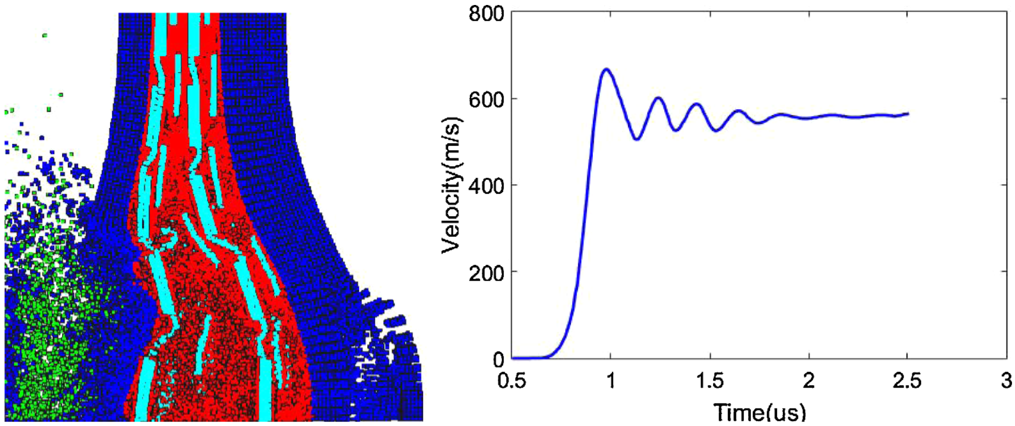


(a) Damage of the impacted sample (b) Particle velocity profile on the rear wall

**Fig. 28.** Simulation results for the hybrid laminate labeled by Al/2C/2Al.

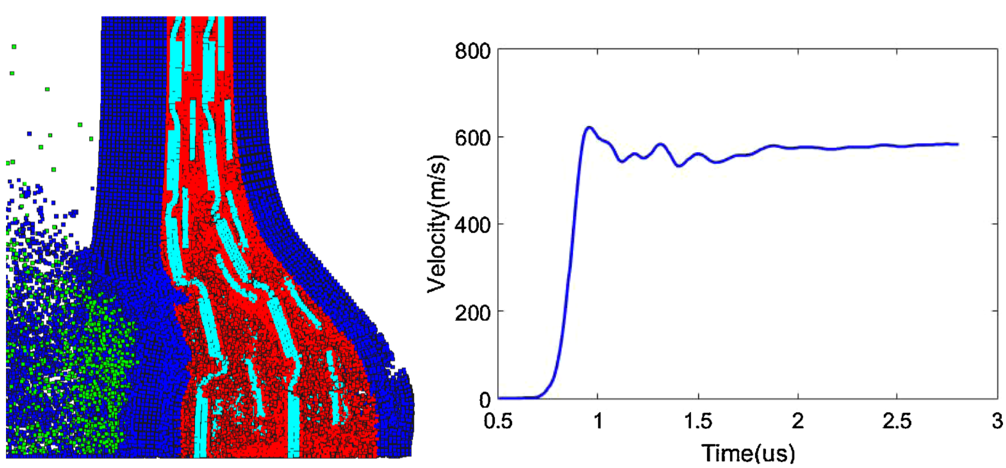


(a) Damage of the impacted sample (b) Particle velocity profile on the rear wall

**Fig. 29.** Simulation results for the hybrid laminate labeled by 2Al/2C/Al.

laminate to remarkably weaken the shock peak owing to its low acoustic impedance in the thickness direction. However, the carbon fiber cannot bear large deformation although it has high tensile strength exceeding 2.0 GPa. Instead, the Kevlar fabric and/or its composite can be selected as an advanced material for HVI protection in view of its low elastic modulus and high strength.

The SPH-based computational model can be directly applied to Kevlar fabric and its composite materials. Compared to the CFRE-sandwiched laminate Al/2C/2Al, we first replace in Fig. 32(b) the sandwiched CFRE layer with Kevlar-fabric and epoxy composite, and then replace half of the rear alloy wall with a 1.0 mm thick Kevlar fabric. It is found that the Kevlar fabric has the better shock wave absorption by large bulge deformation and avoidance of spall film formation from the rear surface.

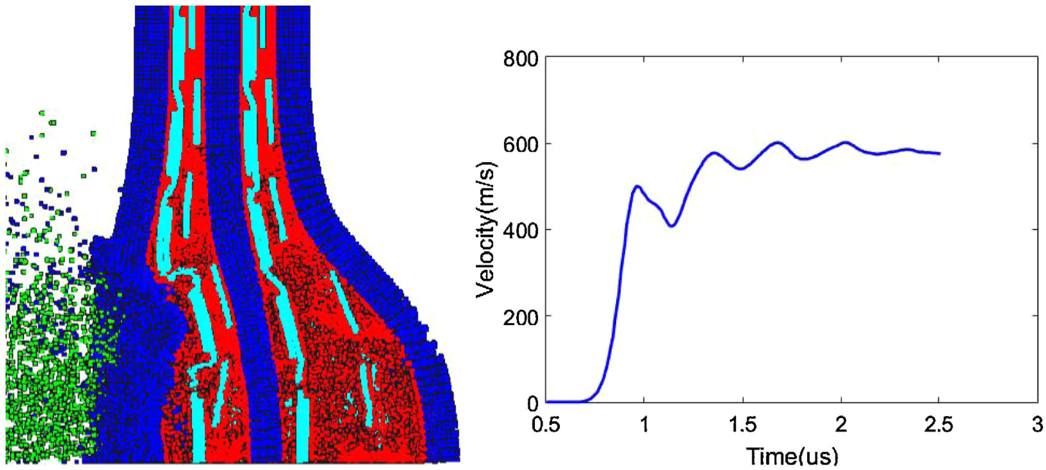


(a) Damage of the impacted sample (b) Particle velocity profile on the rear wall

**Fig. 30.** Simulation results for the hybrid laminate labeled by Al/C/Al/C/Al.

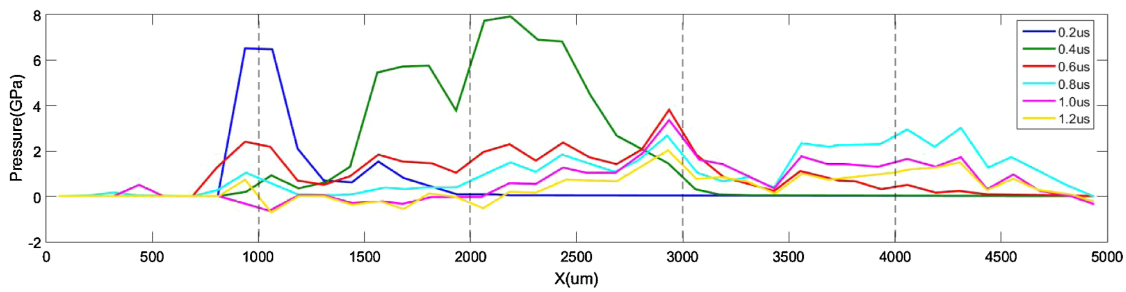


(a) Al/C/Al/C/Al

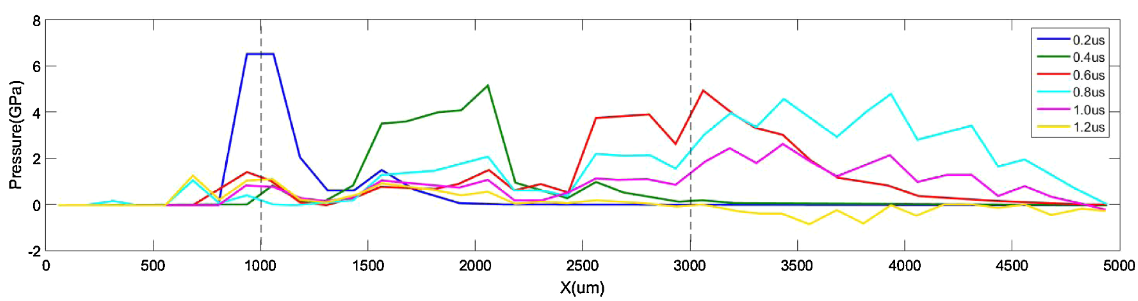


(b) Al/2C/2Al

**Fig.. 31.** Evolution of the shock pressure along the thickness of a hybrid laminate.

It is known that a Whipple shield has much lower areal density than a single laminate for HVI protection. It however may pose a challenge for structural design when a shield has no space to lay out a bumper ahead. The optimization of the hybrid laminate is explored in this work using a corrugated plate and a small gap as shown in Figs. 33. The hybrid laminate applies Kevlar-fabric reinforced epoxy composite as the filler layer and Kevlar fabric as the rear layer.

Figs. 34–36 display damage patterns of the shields, with varying stacking patterns, 20 μs after the HVI of a Mylar film at a velocity 9.0 km/s. The Mylar flyer is 10 mm in diameter and 0.1 mm thick. Compared with a flat front plate, shown in Fig. 34, the corrugated plate would produce an undulated shock wave upon flyer impact, exacerbating to some extent delamination and fracture of the rear Kevlar fabric. But broadening and decay of the shock front, due to the corrugated plate, would be beneficial to the integrity of the rear alloy plate and filler Kevlar composite layer.

If the front alloy plate is prepositioned with a standoff of 1.0mm, as shown in Figs. 35, it would fragment under the short-pulse shock wave resulting from the flyer impact. Although the gap is not large enough for the fragments to spread, the shock wave subsequently formed inside the rear laminate would be attenuated leading to less damage of the Kevlar composite layer and rear alloy plate. Compared with the flat front plate, improvement is observable for the hybrid laminate that uses a corrugated plate.

Provided the shield thickness is restricted to 5.0 mm, the laminate would be laid out in the sequence of a 2024 alloy plate, a gap, a Kevlar reinforced composite layer, a 2024 alloy layer and a Kevlar fabric layer, all with a thickness of 1.0 mm. As shown in Figs. 36(b), the shield using a corrugated front plate and a gap, nearly endures the HVI of a Mylar flyer at 9 km/s. It successfully reduces about one third of the mass in comparison with the hybrid laminate 2Al/2C/Al with the same thickness in Fig. 29.

By comparing between Fig. 35(b) and Fig. 36(b) the damages of the rear alloy/Kevlar layers, it is found that the shielding performance is nearly unchanged even though the latter uses a thinned Kevlar composite layer. The combination of the corrugated plate and a small gap has the advantage of avoiding the formation of a steep and strong shock wave inside a thinned laminate as shown in Fig. 36(b). Advanced

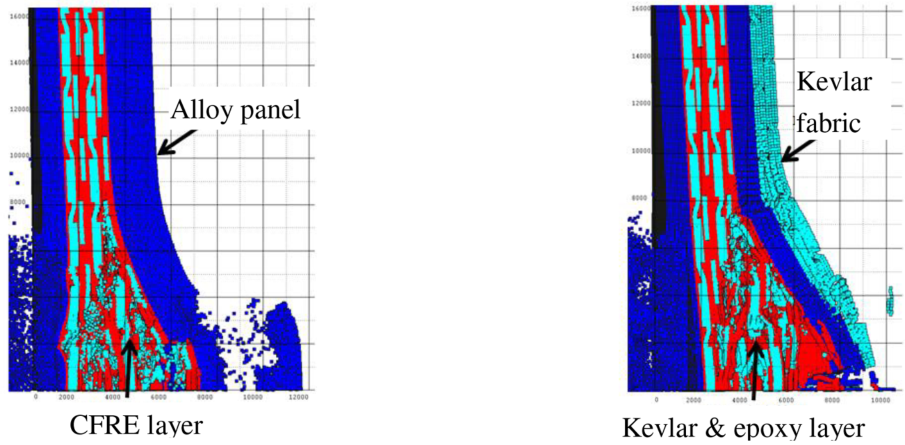


(a) The CFRE and 2024 alloy hybrid laminate (b) The Kevlar and 2024 alloy hybrid laminate

**Fig. 32.** The damage patterns of the CFRE/alloy laminate and the Kevlar/alloy laminates at the time 20 μs after HVI of a 10-mm-diameter and 0.1-mm-thickness Mylar film at a velocity 9.0 km/s.

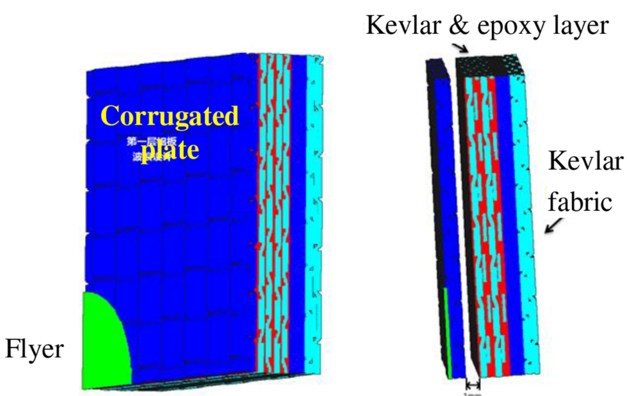


(a) Without a gap (b) With a 1.0mm gap

**Fig. 33.** The computational models for 2024 alloy and Kevlar fabric hybrid laminates using a corrugated front alloy plate.

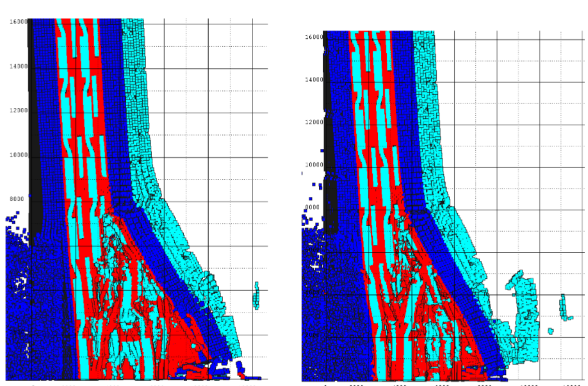

(a)Flat front plate (b)Corrugated front plate

**Fig. 34.** Comparison between the damage patterns of the hybrid laminates with and without use of a corrugated front plate.

fabrics with low modulus and high strength can therefore be activated by producing large deformation and kinetic energy adsorption.

## 5. Discussions and future work

A SPH-based computational model was developed in this work for fiber fabrics and their composite when subjected to HVI. The shielding performance of fabrics with varying fiber properties, weave patterns, and layouts was assessed. As revealed by the simulations, lightweight alloys can form more widely spread debris clouds under HVI, and is thus preferable for their use as bumper materials in a Whipple shield. By contrast, the Nextel fabric would produce fewer fragments in the highest speed range and more fragments at low speeds, being a candidate advanced material for the filler layer of a Whipple shield. Compared with the modulus, the fiber strength plays a more important role in absorbing the kinetic energy of a projectile. The plain weave possesses the best performance in kinetic energy absorption among simulated fabrics, including the twill weave, the parallel-arrange fibers, and the randomly oriented fibers. The 3D orthogonally-woven fabric does not exhibit any advantage over the plain weave both at the projectile velocities of 9.7 km/s and 2.1 km/s, and conversely forms more high speed fragments at the low impact velocity of 2.1 km/s. The influence of pre-compression by formed debris cloud was also examined. We found that the shielding performance of unwoven fabrics can significantly decrease due to the applied pre-compression.

In agreement with previous experimental results, the simulations reveal that the shielding performance of an alloy/FRP hybrid laminate directly correlates with the shock peak decay as it arrives at the rear surface of the laminate. The combination of low-modulus FRP and presence of alloy/FRP interfaces can effectively reduce and spread the shock peak, avoiding localized damage such as spallation. Among the four computed hybrid laminates 2Al/2C/Al, 2Al/C/2Al, 2Al/C/Al, and Al/C/Al/C/Al which have the same thickness of 5.0 mm, the velocity of the first arriving shock peak decayed from 750 m/s for 2Al/C/2Al to 500 m/s for Al/C/Al/C/Al, the latter of which has the best shielding performance under a HVI of a mylar flyer at 9 km/s. In an optimized laminate against HVI, a corrugated plate being prepositioned with a small standoff can further flatten the shock peak, and the residual kinetic energy can then be effectively adsorbed by the use of Kevlar fabric with low-modulus and high-strength. Given the laminate thickness of 5.0 mm, the simulation reveals that this optimized laminate bears the same performance as the laminate 2Al/2C/Al, but has a reduced areal density by 30 percent.

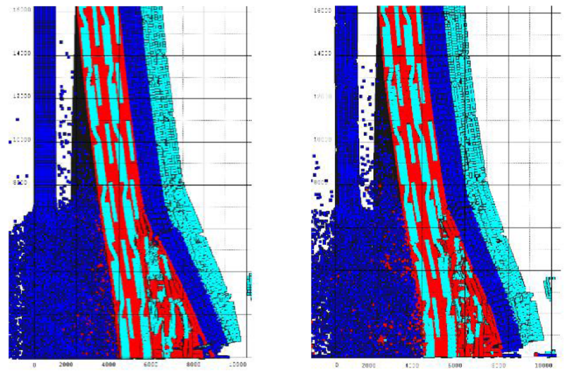

(a) Prepositioned by a flatplate  (b) Prepositioned by a corrugated plate

**Fig. 35.** Comparison between the damage patterns of the hybrid laminates prepositioned, respectively, by a flat plate and a corrugated plate both with a standoff of 1.0 mm.

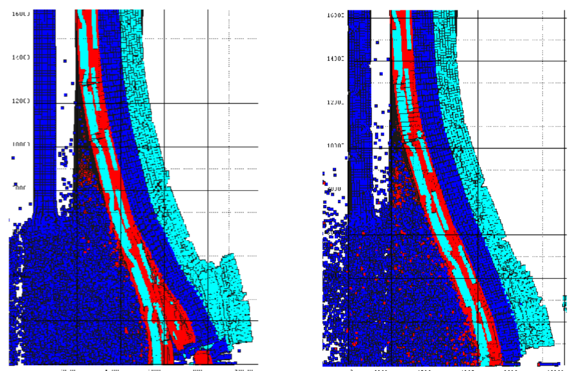

(a) Prepositioned by a flat plate  (b) Prepositioned by a corrugated plate

**Fig. 36.** Optimization of a 5.0 mm thick hybrid laminate with use of a prepositioned corrugated plate.

In an instantaneous HVI process, it is still challenging to establish experimentally a systematic and quantitative scheme for assessing the performance of structural components such as multilayers. Hence, numerical simulations are an effective tool for structural optimization, experimental design, and analyses of experimental measurements. Our SPH-based model builds the reinforced fabric, fiber or strand yarn depending on model scale, and/or the matrix materials by SPH particles. The heterogeneous and anisotropic constitutive relations including plastic deformation and damage can thus be conveniently included. The model is particularly useful for preliminarily estimating the mechanical behaviors of FRP composites, and reproducing shock wave propagation, fracture and fragmentation in composites under HVI provided the fabric/polymer interfacial strength is negligible compared with the applied shock pressure.

As an alternative to the finite element models as developed by Chocron et al [19], the SPH-based model brings a new capability for analyzing and obtaining the constituent and interactive properties of fiber-polymer composite. As a prerequisite for its extension, to application involving medium strain-rates, the fabric/polymer interface response should be incorporated into the computational model in the future work. In this regard, well-developed meshless methods have the advantage of capturing composite texture and enabling particular treatments of the mechanics of interfaces. The second-order precision meshfree algorithm, such as the OTM method reported in [31], however, is still required not only for eliminating the tensile instability among SPH particles, but for properly incorporating interfacial "particles" into the computational model.

## Declaration of Competing Interest

None.

## References


[1] E.L. Christiansen. Meteoroid/Debris Shielding. Technical report TP-2003-210788, 2003.

[2] Destefanis R, Schäfer F, Lambert M, et al. Selecting enhanced space debris shields for manned spacecraft. International Journal of Impact Engineering 2006;33(1-12):219–30.

[3] Tanaka M, Moritaka Y. Single bumper shields based on Vectran fibers. Advances in Space Research 2004;34(5):1076–9.

[4] Christiansen EL, Crews JL, Williamsen JE, et al. Enhanced meteoroid and orbital debris shielding. International Journal of Impact Engineering 1995;17(1-3):217–28.

[5] Christiansen EL, Kerr JH, De la Fuente HM, Schneider WC. Flexible and deployable meteoroid/debris shielding for spacecraft. International Journal of Impact Engineering 1999;23(1):125–36.

[6] Hayhurst CJ, Hiermaier SJ, Clegg RA, Riedel W, Lambert M. Development of Material Models for Nextel and Kevlar-epoxy for High Pressures and Strain Rates. International Journal of Impact Engineering 1999;23(1):365–76.

[7] D. Roylance, S.S. Wang. Penetration mechanics of textile structures. Technical report Natick/TR-80/021, US Army, Natick Research and Development Command. Contract number DAAG17-76-C-0013; 1979.

[8] Novotny WR, Cepus E, Shahkarami A, Vaziri R, Poursartip A. Numerical investigation of the ballistic efficiency of multi-ply fabric armours during the early stages of impact. Int J Impact Eng 2007;34:71–88.

[9] Walker J. Reinecke WG, editor. Constitutive model for fabrics with explicit static solution and ballistic limit 1999:1231–8.

[10] Tan VBC, Ching TW. Computational simulation of fabric armour subjected to ballistic impact. Int J Impact Eng 2006;32:1737–51.

[11] Lim CT, Shim VPW, Ng YH. Finite-element modeling of the ballistic impact of fabric armor. Int J Impact Eng 2003;28(19):13–31.

[12] M. Grujicic, G. Arakere, T. He, M. Gogulapati, B.A. Cheeseman. A numerical investigation of the influence of yarn-level finite-element model on energy absorption by a flexible-fabric armor during ballistic impact. J Mater: Des Appl2008:259–76.

[13] Shahkarami A, Vaziri R. A continuum shell finite element model for impact simulation of woven fabrics. Int J Impact Eng 2007;34:104–19.

[14] Ivanov IV, Tabiei A. Flexible woven fabric micro-mechanical material model with fiber reorientation. Mech Adv Mater Struct 2002;9(1):37–51.

[15] M. Grujicic, W.C. Bell, G. Arakere, T. He, X. Xie, B.A. Cheeseman. Development of a mesoscale material model for ballistic fabric and its use in flexible-armor protection systems. J Mater Eng Perform2010(19–1):22–39.

[16] Rao MP, Duan Y, Keefe M, Powers BM, Bogetti TA. Modelling the effects of yarn material properties and friction on the ballistic impact of a plain-weave fabric. Compos Struct 2009;89(4):556–66.

[17] Chocron S, Ranjan SK, Nicholls AE, Figueroa E, Weiss C, et al. Measurement of strain in fabrics under ballistic impact with embedded nichrome wires: part I: technique. Int J Impact Eng 2009;36(10–11):1296–302.

[18] Chocron S, Figueroa E, King N, Kirchdoerfer T, Nicholls AE, Sagebiel E, Weiss C, Freitas CJ. Modeling and validation of full fabric targets under ballistic impact. Int J Impact Eng 2010;70:2012–22.

[19] Chocron S, Carpenter AJ, Scott NL, Bigger RP, Warren K. Impact on carbon fiber composite: Ballistic tests, material tests, and computer simulations. Int J Impact Eng. 2019;131:39–56.

[20] Chen JK, Allahdadi FA, Carney TC. High-velocity Impact of Graphite/Epoxy Composite Laminates. Composites Science and Technology 1997;57(9-10):1369–79.

[21] Wickleina M, Ryana S, Whiteb DM, Clegg RA. Hypervelocity impact on CFRP: testing, material modelling, and numerical simulation. International Journal of Impact Engineering 2008;35(12):1861–9.

[22] Clegg RA, White DM, Riedel W, Harwick W. Hypervelocity impact damage prediction in composites: Part I - material model and characterization. International Journal of Impact Engineering 2006;33(1-12):190–200.

[23] Riedel W, Nahme H, White DM, Clegg RA. Hypervelocity impact damage prediction in composites: Part II - experimental investigations and simulations. International Journal of Impact Engineering 2006;33(1-12):670–80.

[24] Alexander CS, Key CT, Schumacher SC. Dynamic response and modeling of a carbon fiber-epoxy composite subject to shock loading. J. Appl. Phys. 2013;114:223515.

[25] Lucy LB. A Numerical Approach to the Testing of Fusion Process. The Astronomical Journal 1977;88:1013–24.

[26] Gingold RA, Monaghan JJ. Smoothed Particle Hydrodynamics: Theory and Application to Non-Spherical Stars'. Monthly Notices of the Royal Astronomical Society 1977;181:375–89.

[27] Groenenboom PH. Numerical Simulationof Hypervelocity Impact using the SPHOption in PAM-SHOCK. International Journal of Impact Engineering 1997;20:309–23.

[28] Wan H, Bai SX, Li S, Mo JJ, Zhao SC, Song ZF. Shielding performances of the designed hybrid laminates impacted by hypervelocity flyer. Materials and Design 2013;52:422–8.

[29] Ogi K, Okabe T, Takahashi M, et al. Experimental characterization of high-speed impact damage behavior in a three-dimensionally woven SiC/SiC composite. International Journal of Impact Engineering 2010;41:489.

[30] Katz S, Grossman E, Gouzman I, Murat M, Wiesel E, Wagner HD. Response of composite materials to hypervelocity impact. International Journal of impact Engineering 2008;35(12):1606–11.

[31] Arroyo M, Ortiz M. Local maximum-entropy approximation schemes: A seamless bridge between finite elements and meshfree methods. International Journal for Numerical Methods in Engineering 2006;65:2167–202.

[32] Asay JR, Mix LP, Perry F. Ejection of material from shocked surfaces. Appl Phys Lett 1976(29):284.